

Ulrich Häussler-Combe

Computational Structural Concrete

Theory and Applications

Second Edition



Ernst & Sohn
A Wiley Brand

WILEY

Contents

Preface *V*

List of Examples *XIII*

Notation *XV*

1	Introduction	<i>1</i>
	Why Read This Book?	<i>1</i>
	Topics of the Book	<i>3</i>
	How to Read This Book	<i>5</i>
2	Finite Elements Overview	<i>7</i>
2.1	Modelling Basics	<i>7</i>
2.2	Discretisation Outline	<i>9</i>
2.3	Elements	<i>13</i>
2.4	Material Behaviour	<i>19</i>
2.5	Weak Equilibrium	<i>20</i>
2.6	Spatial Discretisation	<i>22</i>
2.7	Numerical Integration	<i>24</i>
2.8	Equation Solution Methods	<i>26</i>
2.8.1	Nonlinear Algebraic Equations	<i>26</i>
2.8.2	Time Incrementation	<i>28</i>
2.9	Discretisation Errors	<i>31</i>
3	Uniaxial Reinforced Concrete Behaviour	<i>37</i>
3.1	Uniaxial Stress–Strain Behaviour of Concrete	<i>37</i>
3.2	Long–Term Behaviour – Creep and Imposed Strains	<i>45</i>
3.3	Reinforcing Steel Stress–Strain Behaviour	<i>52</i>
3.4	Bond between Concrete and Reinforcement	<i>53</i>
3.5	Smeared Crack Model	<i>56</i>
3.6	Reinforced Tension Bar	<i>59</i>
3.7	Tension Stiffening of Reinforced Bars	<i>64</i>

4	Structural Beams and Frames	67
4.1	Cross-Sectional Behaviour	67
4.1.1	Kinematics	67
4.1.2	Linear Elastic Behaviour	70
4.1.3	Cracked Reinforced Concrete Behaviour	71
4.2	Equilibrium of Beams	81
4.3	Finite Elements for Plane Beams	85
4.3.1	Timoshenko Beam	86
4.3.2	Bernoulli Beam	88
4.4	System Building and Solution	91
4.4.1	Integration	91
4.4.2	Transformation and Assembling	93
4.4.3	Kinematic Boundary Conditions and Solution	95
4.4.4	Shear Stiffness	98
4.5	Creep of Concrete	101
4.6	Temperature and Shrinkage	105
4.7	Tension Stiffening	109
4.8	Prestressing	112
4.9	Large Displacements – Second-Order Analysis	118
4.10	Dynamics	126
5	Strut-and-Tie Models	133
5.1	Elastic Plate Solutions	133
5.2	Strut-and-Tie Modelling	136
5.3	Solution Methods for Trusses	138
5.4	Rigid Plastic Truss Models	145
5.5	Application Aspects	147
6	Multi-Axial Concrete Behaviour	151
6.1	Basics	151
6.1.1	Continua and Scales	151
6.1.2	Characteristics of Concrete Behaviour	153
6.2	Continuum Mechanics	154
6.2.1	Displacements and Strains	154
6.2.2	Stresses and Material Laws	156
6.2.3	Coordinate Transformations and Principal States	157
6.3	Isotropy, Linearity, and Orthotropy	159
6.3.1	Isotropy and Linear Elasticity	159
6.3.2	Orthotropy	161
6.3.3	Plane Stress and Strain	162

6.4	Nonlinear Material Behaviour	164
6.4.1	Tangential Stiffness	164
6.4.2	Principal Stress Space and Isotropic Strength	165
6.4.3	Strength of Concrete	168
6.4.4	Nonlinear Material Classification	172
6.5	Elasto-Plasticity	173
6.5.1	A Framework for Multi-Axial Elasto-Plasticity	173
6.5.2	Pressure-Dependent Yield Functions	178
6.6	Damage	183
6.7	Damaged Elasto-Plasticity	190
6.8	The Microplane Model	192
6.9	General Requirements for Material Laws	199
7	Crack Modelling and Regularisation	201
7.1	Basic Concepts of Crack Modelling	201
7.2	Mesh Dependency	205
7.3	Regularisation	209
7.4	Multi-Axial Smeared Crack Model	216
7.5	Gradient Methods	223
7.5.1	Gradient Damage	223
7.5.2	Phase Field	228
7.5.3	Assessment of Gradient Methods	235
7.6	Overview of Discrete Crack Modelling	236
7.7	The Strong Discontinuity Approach	237
7.7.1	Kinematics	237
7.7.2	Equilibrium and Material Behaviour	240
7.7.3	Coupling	242
8	Plates	249
8.1	Lower Bound Limit State Analysis	249
8.1.1	General Approach	249
8.1.2	Reinforced Concrete Resistance	250
8.1.3	Reinforcement Design	255
8.2	Cracked Concrete Modelling	261
8.3	Reinforcement and Bond	266
8.4	Integrated Reinforcement	273
8.5	Embedded Reinforcement with a Flexible Bond	275

9	Slabs	285
9.1	Classification	285
9.2	Cross-Sectional Behaviour	286
9.2.1	Kinematics	286
9.2.2	Internal Forces	288
9.3	Equilibrium of Slabs	290
9.3.1	Strong Equilibrium	290
9.3.2	Weak Equilibrium	292
9.3.3	Decoupling	294
9.4	Reinforced Concrete Cross-Sections	296
9.5	Slab Elements	298
9.5.1	Area Coordinates	298
9.5.2	Triangular Kirchhoff Slab Element	299
9.6	System Building and Solution Methods	301
9.7	Lower Bound Limit State Analysis	305
9.7.1	Design for Bending	305
9.7.2	Design for Shear	311
9.8	Nonlinear Kirchhoff Slabs	314
9.8.1	Basic Approach	314
9.8.2	Simple Moment–Curvature Behaviour	315
9.8.3	Extended Moment–Curvature Behaviour	318
9.9	Upper Bound Limit State Analysis	322
10	Shells	329
10.1	Geometry and Displacements	329
10.2	Deformations	332
10.3	Shell Stresses and Material Laws	335
10.4	System Building	337
10.5	Slabs and Beams as a Special Case	339
10.6	Locking	341
10.7	Reinforced Concrete Shells	344
10.7.1	Layer Model	344
10.7.2	Slabs As a Special Case	347
11	Randomness and Reliability	353
11.1	Uncertainty and Randomness	353
11.2	Failure Probability	356
11.2.1	Linear Limit Condition	356
11.2.2	Nonlinear Limit Condition	362
11.2.3	Multiple Limit Conditions	367
11.3	Design and Safety Factors	369
11.3.1	Safety Factor Basics	369
11.3.2	Partial Safety Factor Application	373
12	Concluding Remarks	377

	Appendix A Solution Methods	<i>381</i>
A.1	Nonlinear Algebraic Equations	<i>381</i>
A.2	Transient Analysis	<i>384</i>
A.3	Stiffness for Linear Concrete Compression	<i>386</i>
A.4	The Arc Length Method	<i>388</i>
	Appendix B Material Stability	<i>391</i>
	Appendix C Crack Width Estimation	<i>395</i>
	Appendix D Transformations of Coordinate Systems	<i>401</i>
	Appendix E Regression Analysis	<i>405</i>
	References	<i>407</i>
	Index	<i>417</i>

List of Examples

	Page
3.1 Tension bar with localisation	41
3.2 Tension bar with creep and imposed strains	50
3.3 Simple uniaxial smeared crack model	58
3.4 Reinforced concrete tension bar	61
4.1 Moment–curvature relations for given normal forces	80
4.2 Simple reinforced concrete (RC) beam	96
4.3 Creep deformations of RC beam	103
4.4 Effect of temperature actions on an RC beam	107
4.5 Effect of tension stiffening on an RC beam with external and temperature loading	110
4.6 Prestressed RC beam	116
4.7 Stability limit of cantilever column	122
4.8 Ultimate limit for RC cantilever column	123
4.9 Beam under impact load	128
5.1 Continuous interpolation of stress fields with the quad element	135
5.2 Deep beam with strut-and-tie model	141
5.3 Corbel with an elasto-plastic strut-and-tie model	143
6.1 Mises elasto-plasticity for uniaxial behaviour	175
6.2 Uniaxial stress–strain relations with Hsieh–Ting–Chen damage	186
6.3 Stability of Hsieh–Ting–Chen uniaxial damage	188
6.4 Microplane uniaxial stress–strain relations with de Vree damage	196
7.1 Plain concrete plate with notch	207
7.2 Plain concrete plate with notch and crack band regularisation	210
7.3 2D smeared crack model with elasticity	218
7.4 Gradient damage formulation for the uniaxial tension bar	226
7.5 Phase field formulation for the uniaxial tension bar	232
7.6 Plain concrete plate with notch and SDA crack modelling	244
8.1 Reinforcement design for a deep beam with a limit state analysis	258
8.2 Simulation of cracked reinforced deep beam	269
8.3 Simulation of a single fibre connecting a dissected continuum	278
8.4 Reinforced concrete plate with flexible bond	280

	Page
9.1 Linear elastic slab with opening and free edges	303
9.2 Reinforcement design for a slab with opening and free edges with a limit state analysis	309
9.3 Computation of shear forces and shear design	313
9.4 Elasto-plastic slab with opening and free edges	317
9.5 Simple RC slab under concentrated loading	320
9.6 Simple RC slab with yield line method and distributed loading	325
9.7 Simple RC slab with yield line method and concentrated loading	326
10.1 Convergence study for linear simple slab	343
10.2 Simple RC slab with interaction of normal forces and bending	347
11.1 Analytical failure probability of cantilever column	360
11.2 Approximate failure probability of cantilever column with Monte Carlo integration	365
11.3 Simple partial safety factor derivation	373

framework whereby all procedures but for a part of load evaluation remain unchanged.

An alternative and common view of prestressing of beams is based on Eqs. (4.49_{2,3}). We consider the quasi-static case, split internal forces into a part \bullet^ϵ from beam deformation, a part \bullet^p from prestressing and eliminate shear forces

$$-M^{\epsilon''} - M^{p''} = \bar{p}_z \quad (4.166)$$

and furthermore Eq. (4.164) is used leading to

$$-M^{\epsilon''} = \bar{p}_z + (z_p F^p \cos \alpha_p)'' \quad (4.167)$$

A common approximation is $F^p \approx const.$, $\cos \alpha_p \approx 1$ resulting in

$$-M^{\epsilon''} = \bar{p}_z + z_p'' F^p \quad (4.168)$$

wherein $z_p'' F^p$ is a lateral redirection force in the z -direction from the curvature z_p'' of the tendon geometry. This term may be seen as an additional lateral loading counteracting the other loadings (Figure 4.16).

Some characteristic properties of prestressing have to be regarded for the evaluation of σ^p or f^p , respectively.

- Tendon profile parameters z_p, α_p may vary with the beam coordinate x according to prestressing design.
- The prestressing force may vary due to the loss of prestress from friction of the tendon in a conduit.
- Furthermore, a beam deformation may lead to a change in the tendon profile. Two types have to be considered in this context:
 1. *Unbonded prestressing*: total length of the tendon changes. This leads to a global change of the prestressing force.
 2. *Bonded prestressing*: length of the tendon changes locally to keep the geometric compatibility with the concrete. This leads to locally varying changes in the prestressing force.

Two subsequent stages have to be considered for prestressing:

- *Set-up stage* of prestressing with the prescribed prestressing force F_0^p
Prestressing is gradually applied at the beam ends through anchors. The value of F_0^p may vary along the longitudinal beam coordinate x due to friction losses. Such losses have to be determined from prescribed friction coefficients and the curvature of the tendon geometry.
- Tendons may be grouted at the end of the set-up stage leading to *post-bonding*. This is generally denoted as bonded prestressing although this is not entirely precise. Grouting is omitted for unbonded prestressing.
- *Service stage* of prestressing with locked anchors
The prestressing force F_0^p changes into F_p depending on loading and prestressing type.

The tendon geometry plays a key role. It is described for each finite beam element in analogy to the Bernoulli beam trial function (Eq. (4.82)) by

$$z_p = \begin{bmatrix} \frac{r^3}{4} - \frac{3r}{4} + \frac{1}{2} & \frac{L_e r^3}{8} - \frac{L_e r^2}{8} - \frac{L_e r}{8} + \frac{L_e}{8} & \frac{r^3}{4} + \frac{3r}{4} + \frac{1}{2} & \frac{L_e r^3}{8} + \frac{L_e r^2}{8} - \frac{L_e r}{8} - \frac{L_e}{8} \end{bmatrix} \cdot \begin{pmatrix} z_{pI} & \alpha_{pI} & z_{pJ} & \alpha_{pJ} \end{pmatrix}^T \quad (4.169)$$

with the element length L_e and the tendon inclination

$$\alpha_p = \frac{\partial z_p}{\partial x} = \frac{\partial z_p}{\partial r} \frac{\partial r}{\partial x} = z'_p \quad (4.170)$$

Lateral tendon position z_p and inclination α_p at the left-hand and right-hand element nodes are given by z_{pI} , α_{pI} and z_{pJ} , α_{pJ} . The local element coordinate is in the range $-1 \leq r \leq 1$. This approach reproduces $z_p(-1) = z_{pI}$, $z'_p(-1) = \alpha_{pI}$ and $z_p(1) = z_{pJ}$, $z'_p(1) = \alpha_{pJ}$. The geometric length of a tendon within an element e is given by

$$L_e^P = \frac{L_e}{2} \int_{-1}^1 \sqrt{(x'_p)^2 + (z'_p)^2} \, dr \quad (4.171)$$

whereby the derivative of the tendon position x_p in the longitudinal direction has also to be regarded. We obtain

$$x'_p = 1 \quad (4.172)$$

for the nominal undeformed tendon geometry and

$$x'_p = 1 + \epsilon \quad (4.173)$$

considering beam deformations with the longitudinal strain ϵ of the reference axis. Furthermore, on the one hand Eq. (4.169) is applied to the nominal undeformed tendon geometry according to design with

$$\begin{pmatrix} z_{pI} & \alpha_{pI} & z_{pJ} & \alpha_{pJ} \end{pmatrix} = \begin{pmatrix} z_{p0I} & \alpha_{p0I} & z_{p0J} & \alpha_{p0J} \end{pmatrix} \quad (4.174)$$

with prescribed values z_{p0I} , α_{p0I} , z_{p0J} , α_{p0J} . On the other hand, Eq. (4.169) gives the tendon geometry considering beam deformations with

$$\begin{pmatrix} z_{pI} & \alpha_{pI} & z_{pJ} & \alpha_{pJ} \end{pmatrix} = \begin{pmatrix} z_{p0I} + w_I & \alpha_{p0I} + \phi_I & z_{p0J} + w_J & \alpha_{p0J} + \phi_J \end{pmatrix} \quad (4.175)$$

with the beam nodal displacements w_I , ϕ_I , w_J , ϕ_J . This yields z'_p from Eq. (4.169) according to Eq. (4.82₂). The Eq. (4.171) has to be integrated numerically for each element, e.g. with a Gauss integration (Section 2.7). The total length L^P of a tendon is given by adding all element contributions.

Regarding prestressing *without bond* the tendon length can be determined separately with a value L_0^P for the set-up stage and with a value L^P for the service stage whereby Eq. (4.175) is used with the actually calculated nodal displacements for each stage. This has a side effect.

Strains of unbonded tendons do not follow the Bernoulli–Navier hypothesis (Section 4.1.1).

The prestressing force is prescribed with F_0^p for the set-up stage and is determined with

$$F^p = \frac{L^p}{L_0^p} F_0^p \quad (4.176)$$

in the service stage of prestressing.

Regarding prestressing with *post-bonding* a tendon gets a *local* elongation after locking of prestressing anchors and grouting due to bond between tendons and concrete. This local elongation is ruled by the beam deformation kinematics (Eq. (4.5)) and the additional strain of the tendon is given by

$$\Delta\epsilon_p(x) = \Delta\epsilon(x) - z_p \Delta\kappa(x) \quad (4.177)$$

with the difference $\Delta\epsilon$, $\Delta\kappa$ of generalised strains between set-up and service stage whereby varying along the beam axis.

Strains of post-bonded tendons follow the Bernoulli–Navier hypothesis during the service stage although not during the set-up stage.

This leads to a prestressing force

$$F^p(x) = F_0^p + E_p A_p \Delta\epsilon_p(x) \quad (4.178)$$

in the service stage with Young's modulus E_p of the prestressing steel – elastic behaviour is assumed to simplify – and the cross-sectional area A_p of tendons.

Finally, internal prestressing forces contributing to loadings are determined using Eq. (4.164). A loading from prestressing distinguishes from self weight, service load, temperature as it depends on displacements and yields a nonlinear load contribution. But the computations show that F^p and F_0^p generally do not differ by large amounts. Thus, the particular procedures concerning prestressing can be summarised with

- define the tendon geometry and prestressing force,
- compute internal forces from prestressing,
- compute nodal forces from prestressing and apply as loads,
- compute system reaction,
- iterate if necessary to consider a change in prestressing forces

which seamlessly fits into the incrementally iterative approach (Section 2.8.2). The application is demonstrated with the following example.

Example 4.6: Prestressed RC beam

We refer to Example 4.2 with basically the same system, but the span is doubled to $L = 10$ m. Thus, load bearing capacity is strongly reduced. Prestressing is used to maintain this capacity. The relevant system parameters are as follows:

- A concrete cross-section $b = 0.2$, $h = 0.4$, a compressive strength $f_{cd} = 38$ MN/m² and a lower and upper reinforcement $A_{s1} = A_{s2} = 12.57$ cm², $d_1 = d_2 = 5$ cm yield an ultimate bending moment $M_u \approx 0.20$ MNm with $N = 0$ (Example 4.1, Figure 4.4). This corresponds to an uniform loading $q_u = 8M_u/L^2 = 15.2$ kN/m which should be increased by prestressing.
- A nominal uniform concrete prestressing stress of $\sigma_{c0} = -10$ MN/m² is chosen in a first approach leading to $F_0^p = 0.8$ MN. The nominal tendon geometry of the whole beam is given by a parabola starting and ending in the centre line with a downward catenary h_p . This is described by

$$z_p = 4h_p \left(\frac{x^2}{L^2} - \frac{x}{L} \right) \quad (4.179)$$

A value $h_p = 0.15$ m is chosen in this example.

- Prestressing tendon and steel properties are chosen with cross-sectional area $A_p = 6$ cm², elastic limit $f_{p0,1} = 1600$ MN/m², strength $f_p = 1800$ MN/m², Young's modulus $E_p = 200\,000$ MN/m², nominal initial steel stress $\sigma_0^p = 1333$ MN/m² with a strain $\epsilon_0^p = 6.67$ ‰.
- A dead load is assumed with $q = 5$ kN/m.

Loading is applied in two steps: (1) set-up of prestressing and dead load, (2) locking of prestressing and additional application of a service load $q_p = 25$ kN/m. Frictional losses are neglected to simplify this example. Both cases – prestressing with and without bond – are alternatively regarded for the service stage of prestressing. The solution method is incrementally iterative with Newton–Raphson iteration within increments. This leads to the following results for prestressing *without* bond:

- The computed increase in prestressing force after load step 2 according to Eq. (4.176) is minimal with $F^p/F_0^p = 1.002$. This results from the low ratio $h_p/L = 1/67$.
- For the computed mid-span displacements, see Figure 4.17a. The deflection starts with an uplift during application of prestressing. The final mid-span deflection in load step 2 is quite large with 0.107 m ($\approx 1/90$ of the span), but the load-carrying capacity is not yet exhausted with an upper mid-span concrete compressive strain of -2.0 ‰ (limit strain is -3.5 ‰). Serviceability is presumably not given without further provisions due to the high slenderness (1/25).
- For the bending moment M_c in the RC cross-section only see Figure 4.18a. The total moment from the dead load and the service load is $M_q = 0.03 \cdot 10^2/8 = 0.375$ MNm. The computed RC mid-span contribution is $M_c = 0.255$ and the contribution from prestressing $M_p = 0.120$. The increased RC moment compared to the initial estimation results from the compressive normal force.

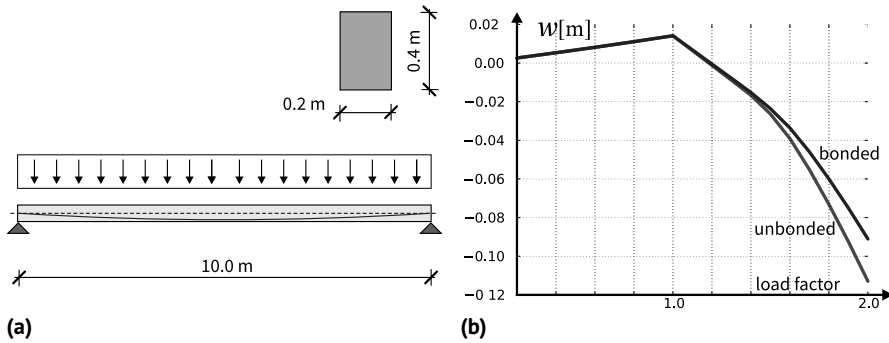


Figure 4.17 Example 4.6. (a) System. (b) Mid-span load–deflection curve.

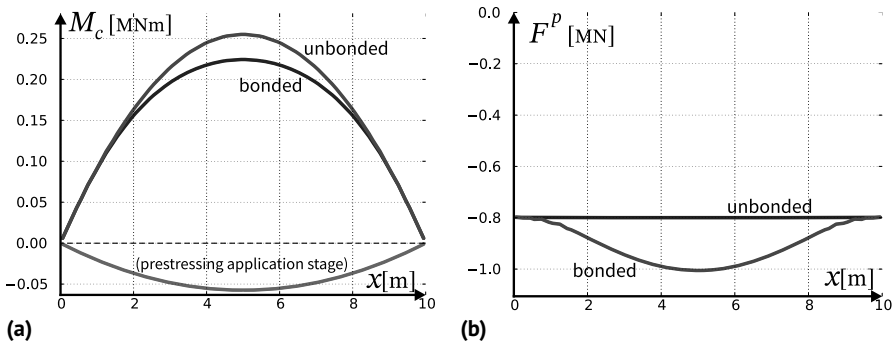


Figure 4.18 Example 4.6. Final stage. (a) RC bending moment M_c . (b) Prestressing force F^p .

Furthermore, the results for prestressing *with* post-bonding:

- The tendon gets a local additional strain due to the locally varying deformation of the beam (Eq. (4.177)). This leads to an additional prestressing force F^p , see Eq. (4.178) and Figure 4.18b, and to a higher contribution of prestressing to the load bearing capacity whereby reducing concrete demand.
- More significant results are given with the final mid-span deflection reduced to 0.086 m (Figure 4.17b) compared to the unbonded case, the RC moment contribution reduced to $M_c = 0.220$ (Figure 4.18a) and the prestressing moment contribution increased to $M_p = 0.155$.

Prestressing roughly leads to a doubling of ultimate limit loads in this example. Aspects of serviceability have to be treated separately. The comparison between prestressing with and without bond in this example is somehow academic, as in practice prestressing with bond is exposed to more non-mechanical effects which might lead to some restrictions to fully utilise the load carrying capacities of the prestressing steel. Details are ruled in codes.

Finally, the uniaxial stress–strain relations are derived for the two material symmetry directions. The 1-direction has $\sigma_{22} = 0$, leading to

$$\sigma_{11} = E_1 \epsilon_{11}, \quad \epsilon_{22} = -\frac{\bar{\nu}}{\sqrt{E_1 E_2}} \sigma_{11} \quad (6.35)$$

With given values for σ_{11} , ϵ_{11} , ϵ_{22} from a test *A*, two equations are given for three unknowns E_1 , E_2 , $\bar{\nu}$. The 2-direction has $\sigma_{11} = 0$ leading to

$$\sigma_{22} = E_2 \epsilon_{22}, \quad \epsilon_{11} = -\frac{\bar{\nu}}{\sqrt{E_1 E_2}} \sigma_{22} \quad (6.36)$$

With given values for σ_{22} , ϵ_{22} , ϵ_{11} from a test *B* – strains from test *A* and test *B* are not the same – two further equations are given for the unknown material parameters. Thus, the set of four equations (6.35) and (6.36) is overdetermined for the unknowns E_1 , E_2 , $\bar{\nu}$. A best fit may be found with a least squares approach (Appendix E, Eqs. (E.2)–(E.6)).

6.4 Nonlinear Material Behaviour

6.4.1 Tangential Stiffness

With respect to the uniaxial case, nonlinear material behaviour of concrete is characterised by a decreasing tangential material stiffness (Figure 3.1). This property is transferred to the multi-axial case. A general formulation of nonlinear material behaviour is given by Eq. (6.12)

$$\dot{\sigma} = \mathbf{C}_T \cdot \dot{\epsilon} \quad (6.37)$$

With respect to the initial behaviour of previously unloaded concrete, it can be assumed that it initially behaves as a linear elastic isotropic material. The initial tangential material stiffness matrix \mathbf{C}_T is given according to Eq. (6.23). Values for the initial Young's modulus E_c and the initial Poisson's ν ratio depending on concrete grade are given by EN 1992-1-1 (2004, 3.1.3), CEB-FIP2 (2012, 5.1.7). But a tangential stiffness matrix \mathbf{C}_T is subject to change after the initial state and may depend on stress σ , strain ϵ and internal state variables κ

$$\mathbf{C}_T = \mathbf{C}_T(\sigma, \epsilon, \kappa) \quad (6.38)$$

Internal state variables κ comprise a loading history. They are necessary, as an actual state σ, ϵ may lead to different responses $\dot{\sigma}$ for different loading histories with a given $\dot{\epsilon}$. Internal state variables require *evolution laws*

$$\dot{\kappa} = \mathcal{F}(\sigma, \epsilon, \kappa) \quad (6.39)$$

describing their rates depending on stress, strain, and values of internal state variables.

Aspects of isotropy and anisotropy as were described in Section 6.3 are also an issue for nonlinear behaviour. Isotropic nonlinear behaviour is characterised in the same way as was formulated in Section 6.3.1. The previous reasoning regarding σ , ϵ in the same way applies to rates $\dot{\sigma}$, $\dot{\epsilon}$, leading the same conclusion about the principal directions of the stress and strain rates and to the same restrictions for the coefficients of an isotropic tangential material stiffness \mathbf{C}_T

← A *nonlinear isotropic* material behaves in the same way in every action direction. Principal directions of stress *increments* coincide with principal directions of strain *increments* for a given material state. The principal stress increments have the same values for all principal strain directions with given strain increment values.

In analogy to Eq. (6.20), an isotropic tangential material stiffness matrix obeys a relation

$$\mathbf{C}_T = \mathbf{Q}^T \cdot \mathbf{C}_T \cdot \mathbf{Q} \quad (6.40)$$

for arbitrary rotations \mathbf{Q} . As a consequence, the tangential material stiffness matrix \mathbf{C}_T has to follow a form like Eq. (6.22), which allows only for two independent coefficients.

Materials initially isotropic may become anisotropic in higher loading levels. In the case of concrete a *load-induced anisotropy* especially arises with cracking whereby the direction normal to a crack has a reduced capacity to transmit tensile stresses while stiffness and strength may remain unaffected in the direction of a crack (Figure 3.3a).

Orthotropic forms may be used to model a load-induced anisotropy due to cracking. The tangential material stiffness matrix \mathbf{C}_T then has to obey to a form like Eq. (6.25) or Eq. (6.34) in the case of plane stress and shear isotropy. The respective matrix coefficients may depend on stress, strain, and loading history according to Eq. (6.38). The orthotropic tangential material flexibility \mathbf{D}_T for 3D states gets a form according to Eq. (6.26) with varying coefficients. Corresponding forms are derived in Section 7.4 within the framework of 2D smeared crack models (Section 3.5).

6.4.2 Principal Stress Space and Isotropic Strength

Stress limit states mark the other end compared to initial states. They describe the *strength* of materials. For initially isotropic materials like concrete, such *stress limit states* are described by an isotropic *strength condition*

$$g(I_1, J_2, J_3) = 0 \quad (6.41)$$

using stress invariants I_1, J_2, J_3 derived from principal stress values $\sigma_1, \sigma_2, \sigma_3$ by Eq. (6.19). Stress states with $g(I_1, J_2, J_3) \leq 0$ are admissible; states $g(I_1, J_2, J_3) > 0$ cannot be sustained. This has some implications.

- The orientation of principal stress directions relative to material directions (Section 6.3) has no influence on the strength condition.

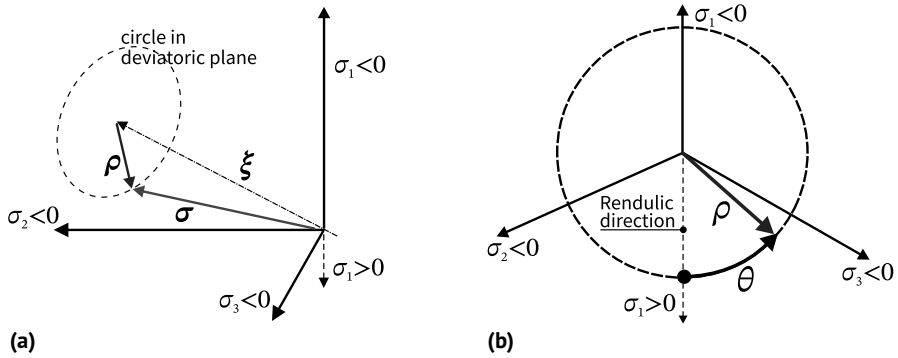


Figure 6.4 (a) Hydrostatic length and deviatoric plane. (b) Deviatoric length and Lode angle in the deviatoric plane.

- Furthermore, an exchange of principal stress values (Section 6.2.3) does not have any influence on the strength condition either.
- Admissible forms for equivalent functions $f(\sigma_1, \sigma_2, \sigma_3)$ derived from $g(I_1, J_2, J_3)$ by using Eq. (6.19) are constrained by the inherent structure of the invariants.

We assume the admissible forms $f(\sigma_1, \sigma_2, \sigma_3)$ for the following.

The stress–strain behaviour described by Eq. (6.37) is sometimes separated from the strength limit states described by $f(\sigma_1, \sigma_2, \sigma_3)$, and both are treated independently. To have a consistent material description the integration of stresses σ from Eq. (6.37) during the loading history driven by a time t should not lead to stress states violating the strength condition Eq. (6.41). The elasto-plastic material models described in Section 6.5, the damage models described in Section 6.6, or the microplane models described in Section 6.8 combine stress–strain relations and strength in such a way that the consistency of the material description is ensured.

An isotropic strength condition generally becomes active with one predominant principal stress component. Let us assume that σ_1 activates the tensile strength in the 1-direction. The respective material point is generally not considered to fail in every aspect. A utilisation of strength in the remaining directions is still allowed in the following loading history. Thus, e.g. a load-induced anisotropy – tensile strength is reached in one direction, while compressive strength is utilised in orthogonal directions – may be combined with an isotropic strength condition.

◀ Isotropic strength conditions basically do not exclude *anisotropic* stress–strain relations.

Such isotropic strength conditions $f(\sigma_1, \sigma_2, \sigma_3)$ are used for concrete and will be considered in the following.

Principal stress values span a triaxial Cartesian coordinate system (\rightarrow principal stress space), and the corresponding stress state is given by a vector. This has the following significant elements, see also Figure 6.4:

- The hydrostatic axis as a space diagonal with a direction $\mathbf{n}_\xi = (1 \ 1 \ 1)^T / \sqrt{3}$. A direction is a vector of length 1 by definition.
- The projection of a stress vector $\boldsymbol{\sigma} = (\sigma_1 \ \sigma_2 \ \sigma_3)^T$ on the hydrostatic axis: $\boldsymbol{\xi} = \xi (1 \ 1 \ 1)^T / \sqrt{3}$ with hydrostatic length $\xi = (\sigma_1 + \sigma_2 + \sigma_3) / \sqrt{3}$.
- The deviatoric plane with origin at $\boldsymbol{\xi}$ and a normal \mathbf{n}_ξ . It is spanned by all vectors starting in $\boldsymbol{\xi}$ with zero hydrostatic length ξ .
- The projection of a stress vector $\boldsymbol{\sigma} = (\sigma_1 \ \sigma_2 \ \sigma_3)^T$ on its deviatoric plane

$$\boldsymbol{\rho} = \boldsymbol{\sigma} - \boldsymbol{\xi} = \frac{1}{3} \begin{pmatrix} 2\sigma_1 - \sigma_2 - \sigma_3 \\ -\sigma_1 + 2\sigma_2 - \sigma_3 \\ -\sigma_1 - \sigma_2 + 2\sigma_3 \end{pmatrix} \quad (6.42)$$

with $\rho_1 + \rho_2 + \rho_3 = 0$.

- The projection of the particular vector $\boldsymbol{\sigma} = (1 \ 0 \ 0)^T$ on the deviatoric plane according to Eq. (6.42): $\boldsymbol{\rho}_1 = 2/3 (1 \ -\frac{1}{2} \ -\frac{1}{2})^T$. It has a direction $\bar{\boldsymbol{\rho}}_1 = \sqrt{2/3} (1 \ -\frac{1}{2} \ -\frac{1}{2})^T$ called the Rendulic direction in the following.

An isotropic strength condition like Eq. (6.41) forms a *strength surface* in the principal stress space and defines triaxial strength. A stress vector and, in particular, a point on this surface can be described by *Haigh–Westergaard coordinates* with the following components:

- The *hydrostatic length* ξ is already introduced as length of the stress vector on the hydrostatic axis

$$\xi = \frac{1}{\sqrt{3}} (\sigma_1 + \sigma_2 + \sigma_3) = \frac{I_1}{\sqrt{3}} \quad \rightarrow \quad I_1 = \sqrt{3} \xi \quad (6.43)$$

- The *deviatoric length* ρ results from the length of the vector $\boldsymbol{\rho}$ from Eq. (6.42). This leads to the second invariant of the stress deviator (Eq. (6.19))

$$\rho = |\boldsymbol{\rho}| = \sqrt{2J_2} \quad \rightarrow \quad J_2 = \frac{\rho^2}{2} \quad (6.44)$$

- The *Lode angle* θ spans between the Rendulic direction and deviatoric direction

$$\cos \theta = \frac{1}{\rho} \boldsymbol{\rho} \cdot \bar{\boldsymbol{\rho}}_1 \quad (6.45)$$

A common alternative of this formulation is given by

$$\cos 3\theta = 4 \cos^3 \theta - 3 \cos \theta = \frac{3\sqrt{3}}{2} \frac{J_3}{\sqrt{J_2^3}} \quad (6.46)$$

with the second and third invariants J_2, J_3 of the stress deviator (Eq. (6.19)). Equation (6.46) yields one solution in the range $0^\circ \leq \theta \leq 60^\circ$. But this is not a restriction, as any interchanging of $\sigma_1, \sigma_2, \sigma_3$ is equivalent; see the remarks following Eq. (6.41).

A convention

$$\sigma_1 \geq \sigma_2 \geq \sigma_3 \quad (6.47)$$

(signed!) is generally used without loss of generality with respect to isotropic strength. Thus, a state of stress is uniquely determined by ξ , ρ and, finally, θ in the range $0 \leq \theta \leq 60^\circ$.

6.4.3 Strength of Concrete

The strength of solid materials is determined experimentally with specimens of at least the size of an representative volume element (RVE) (Section 6.1.1). Cylindrical specimens are often used for concrete. A typical experimental set-up is shown in Figure 6.5 with the *triaxial cell*.

It allows applying longitudinal and radial pressure independently from another. The radial pressure is connected with a circumferential pressure of the same value to establish equilibrium. Both form the confining pressure. A first principal stress directly corresponds to the longitudinal pressure; the confining pressure leads to the identical second and third principal stress. A test is started with identical longitudinal and confining pressures. After that, the longitudinal pressure is changed until it reaches an extremal value corresponding to strength. Such a set-up has the following locations in the principal stress space:

- The *compressive meridian* with $\sigma_1 = \sigma_2 > \sigma_3$ (signed): a cylindrical specimen with compression $\sigma_3 < 0$ in the longitudinal direction and circumferential confining pressure $\sigma_1 = \sigma_2 < 0$, $|\sigma_1| < |\sigma_3|$. Equation (6.19) yields $J_2 = (\sigma_1 - \sigma_3)^2/3$ and $J_3 = -2(\sigma_1 - \sigma_3)^3/27$ and Eq. (6.46) $\cos 3\theta = -1$ or $\theta = 60^\circ$.
- The *tensile meridian* with $\sigma_1 > \sigma_2 = \sigma_3$ (signed): a cylindrical specimen with circumferential confining pressure $\sigma_2 = \sigma_3 < 0$ and a longitudinal compression $\sigma_1 < 0$, $|\sigma_1| < |\sigma_3|$. Equation (6.19) yields $J_2 = (\sigma_1 - \sigma_3)^2/3$ and $J_3 = 2(\sigma_1 - \sigma_3)^3/27$ and Eq. (6.46) $\cos 3\theta = 1$ or $\theta = 0^\circ$.

The compressive and tensile meridians form particular curves within the strength surface as is shown in Figure 6.6. They are determined as the intersection of the strength surface with the deviatoric planes with Lode angles $\theta = 60^\circ$ and $\theta = 0^\circ$, re-

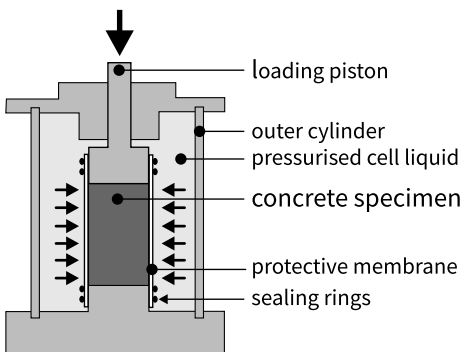


Figure 6.5 Triaxial cell.

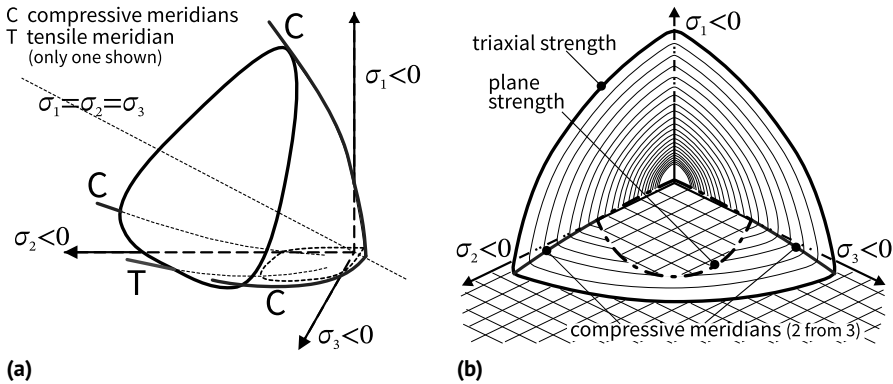


Figure 6.6 Strength surfaces. (a) General view direction. (b) Pressure axis view direction.

spectively. Strength surfaces of concrete themselves form a smoothed, curved tetrahedron (Figure 6.6). Its tip is located in the positive octant ($\sigma_1 > 0, \sigma_2 > 0, \sigma_3 > 0$) near the origin. The origin indicates the triaxial tensile strength. The strength surface opens in the negative octant ($\sigma_1 < 0, \sigma_2 < 0, \sigma_3 < 0$) and can be specified as follows:

- Many experimental data exist for the compressive and the tensile meridians due to the relatively simple triaxial cell set-up (Figure 6.5). Both meridians are slightly curved. The tensile meridian falls below the compressive meridian, if both are sketched in a plane.
- The range between compressive and tensile meridians with a Lode angle $0^\circ \leq \theta \leq 60^\circ$ is sufficient to describe the whole strength surface. This section replicates for the remaining range full range of θ due to the isotropic strength condition; see the remarks following Eq. (6.41). This also replicates the meridians.
- The range $0^\circ \leq \theta \leq 60^\circ$ has three different principal stresses, which cannot be realised with the conventional triaxial cell according to Figure 6.5. True triaxial cells are required with a much higher experimental effort, and experimental data are rare in this range (Hampel et al. 2009).
- Strength 'increases' under hydrostatic pressure. Or more precisely, the admissible deviatoric length increases with increasing pressure for a certain range of pressures. This also depends on the Lode angle.
- The deviatoric concrete strength under very high pressures is not really known yet. From a theoretical point of view, there is no strength limit for a pure pressure. Practically, pure pressure is not reachable in experimental set-ups. Small deviatoric parts cannot be avoided.
- The tensile strength in multi-axial tension does not significantly differ from uniaxial tensile strength. Thus, it should be possible to reach the uniaxial tensile strength in three directions simultaneously. But this has not yet been proved experimentally up to now.

A stress–strain relation has to be defined for all states within the strength surface. This may be assumed as isotropic linear elastic initially and become increasingly

nonlinear when approaching the strength surface. Basic approaches to describe nonlinear material behaviour are given with elasto-plasticity described in Section 6.5, damage described in Section 6.6, and microplane described in Section 6.8.

A selection of widely referenced formulations for the strength surface of concrete is given in the following.

- The strength surface of *Ottosen* (Ottosen 1977)

$$f = a \frac{J_2}{f_c^2} + \lambda \frac{\sqrt{J_2}}{f_c} + b \frac{I_1}{f_c} - 1 = 0 \quad (6.48)$$

with the uniaxial compression strength f_c (unsigned), constants a, b , and

$$\begin{aligned} \lambda &= k_1 \cos \left[\frac{1}{3} \arccos(k_2 \cos 3\theta) \right], & \text{for } \cos 3\theta \geq 0 \\ \lambda &= k_1 \cos \left[\frac{\pi}{3} - \frac{1}{3} \arccos(-k_2 \cos 3\theta) \right], & \text{for } \cos 3\theta \leq 0 \end{aligned} \quad (6.49)$$

with further constants k_1, k_2 . The four material constants a, b, k_1, k_2 are determined from the tensile strength f_{ct} , the biaxial strength, and points on the compressive meridian.

- The strength surface of *Hsieh-Ting-Chen* (Hsieh et al. 1982)

$$f = a \frac{J_2}{f_c^2} + b \frac{\sqrt{J_2}}{f_c} + c \frac{\sigma_1}{f_c} + d \frac{I_1}{f_c} - 1 = 0 \quad (6.50)$$

with constants a, b, c, d and the largest principal stress σ_1 . This is rewritten as

$$f = \bar{a} \left(\frac{\rho}{f_c} \right)^2 + (\bar{b} \cos \theta + \bar{c}) \frac{\rho}{f_c} + \bar{d} \frac{\xi}{f_c} - 1 = 0 \quad (6.51)$$

with the hydrostatic length ξ (Eq. (6.43)), the deviatoric length ρ (Eq. (6.44)), and Lode angle θ (Eq. (6.46)). Hence, the largest principal stress σ_1 is replaced by invariants.

- The strength surface of *Willam/Warnke* (Willam and Warnke (1975), Chen and Saleeb (1994, Section 5.5)).

$$\bar{\rho} = \frac{2\rho_c(\rho_c^2 - \rho_t^2) \cos \theta + \rho_c(2\rho_t - \rho_c) \sqrt{4(\rho_c^2 - \rho_t^2) \cos^2 \theta + 5\rho_t^2 - 4\rho_t\rho_c}}{4(\rho_c^2 - \rho_t^2) \cos^2 \theta + (\rho_c - 2\rho_t)^2} \quad (6.52)$$

with

$$\bar{\xi} = a_0 + a_1 \rho_t + a_2 \rho_t^2, \quad \bar{\xi} = b_0 + b_1 \rho_c + b_2 \rho_c^2 \quad (6.53)$$

and $\bar{\xi} = \xi/f_c$, $\bar{\rho} = \rho/f_c$. The parameters ρ_t describe the normalised tensile meridian, i.e. $\theta = 0^\circ$ and ρ_c the normalised compressive meridian, i.e. $\theta = 60^\circ$. The parameters $a_0, a_1, a_2, b_0, b_1, b_2$ are material constants. As the compressive and